Quantum States of the Endohedral Fullerene Li@C_{60}

Ming Zhang,[†] Lawrence B. Harding,[‡] Stephen K. Gray,*[,‡] and Stuart A. Rice*[,†]

Department of Chemistry and James Franck Institute, University of Chicago, Chicago, Illinois 60637, and Chemical Sciences and Engineering Division, Argonne National Laboratory, Argonne, Illinois 60439

Received: February 5, 2008; Revised Manuscript Received: March 25, 2008

We present a theoretical study of the eigenstates of the endohedral fullerene Li@C_{60} for the case that the C_{60} cage is assumed to be stationary. These eigenstates represent the three-dimensional nuclear dynamics of a Li atom confined to the interior of the carbon cage. The potential function employed, based on density functional theory calculations that we performed, has a variety of minima corresponding to complex hindered rotations of the Li atom in a shell about 1.5 Å from the cage center. The energies and wave functions of the lowest 1200 states have been calculated, and the characteristic features of selected states and the far-IR spectrum are discussed. An interesting result of the calculations is the finding that the ground-state eigenfunction can become strongly localized when the cage atoms are just slightly perturbed from icosahedral symmetry.

1. Introduction

Endohedral fullerenes consist of atoms, molecules, or clusters encapsulated by a fullerene.[1–3] A fascinating array of such complexes have been prepared and studied, many of which exhibit potentially useful properties. For example, the metallofullerene La_2@C_{80} has been shown to act as a field-effect transistor,[4] and the long spin lifetimes in N@C_{60} suggest that it may be useful as a qubit in a quantum computer.[5] Actual practical applications based on these systems have yet to be developed, in part because of the low yields of the physical methods used for their synthesis (e.g., vaporization). However, an organic synthesis of H_2@C_{60} has been reported,[6] which suggests that when chemical synthesis methods are further developed, there is hope that other endohedral fullerenes will eventually be prepared in greater quantities.

Although it is therefore unclear whether endohedral fullerenes will find practical use, the unique structures of these systems make them ideal for studying how nanoscale confinement can alter the spectroscopy and dynamics from that expected in bulk matter. Indeed, very complex nanostructures can now be created by using a variety of procedures. Understanding how atoms and molecules behave in or on these nanostructures is of both fundamental and practical relevance. For example, it has been suggested that molecules trapped inside carbon nanotubes may, through quantum confinement effects, be selectively sieved.[7,8] Confinement effects in carbon nanotubes may also lead to an enhanced chemical reactivity of the trapped species.[9,10]

The focus of this paper is a detailed study of the quantum mechanical bound states of a three-dimensional model for a Li atom moving inside a C_{60} cage, Li@C_{60}. Our work is similar in spirit to a recent quantum mechanical study of H_2@C_{60}[11] that pointed to a variety of interesting spectroscopic consequences arising from the confinement. There have been some experimental[12–14] and theoretical[15–17] studies of Li@C_{60}. The theoretical calculations[15,16] suggest that the ground electronic state is ionic in nature and is essentially composed of a Li^+ ion in a C_{60}^- cage. The equilibrium position of Li is not at the center of the cage; the Li is displaced from the center of symmetry of the C-atom cage by more than 1 Å. This structure is typical of endohedral metallofullerenes and is in contrast with the structures of endohedral fullerenes with less polarizable, neutral dopants, including H_2@C_{60}, where the dopant atom or molecule lies at the cage center. Li may be thought of as vibrating radially about its equilibrium position while undergoing hindered rotational motion in a spherical shell. Some interesting properties of the patterns of the hindered rotational levels for several related endohedral fullerenes, based on a simple parametrization of a two-dimensional model, were discussed in ref 17.

In this work, we develop a potential-energy function for Li@C_{60} based on density functional theory (DFT) calculations and determine numerous ro-vibrational energies and eigenfunctions of a three-dimensional model that allows the Li to move but keeps the C atoms fixed. We discuss the nature of selected eigenfunctions and the far-IR spectrum estimated from all the wave functions. We also discuss an unusual result that emerges from the calculations, namely, how small perturbations of the C-atom positions can dramatically localize the wave function.

2. Theoretical Model and Computational Methods

The Hamiltonian operator for Li@C_{60} is taken to be

$$\hat{H} = -\frac{\hbar^2}{2m}\left(\frac{\partial^2}{\partial x^2}+\frac{\partial^2}{\partial y^2}+\frac{\partial^2}{\partial z^2}\right)+V(x,y,z) \qquad (1)$$

where $m = 7.016$ amu is the mass of ^{7}Li and (x, y, z) denotes the position of Li relative to the center of the C_{60} cage. In what follows, we outline how we determine the potential $V(x, y, z)$ (Section 2.1) and eigenstates (Section 2.2).

2.1. Electronic-Structure Calculations and Potential-Energy Function. The potential-energy surface for the motion of the Li atom within a rigid symmetrical C_{60} cage was calculated by using B3LYP/6-311G(d) DFT. These calculations represent a significant improvement over the previous LDA DFT calculations on this system[15,16] but are still not expected to be of spectroscopic accuracy. The Cartesian coordinates for each C atom in the cage were obtained analytically with the procedure of ref 18, and the electronic-structure calculations were carried out with the GAUSSIAN98 program.[19] The potential was

* Corresponding authors. E-mail: gray@tcg.anl.gov (S.K.G.), s-rice@uchicago.edu (S.A.R.).
† University of Chicago.
‡ Argonne National Laboratory.

10.1021/jp801083m CCC: $40.75
Published on Web 05/21/2008

TABLE 1: Potential-Energy Function Parameters and Normal-Mode Frequency Analysis around the Hexagonal and Pentagonal Potential Wells

potential-function parameters		
D_e	α_e	s_e
506.965 cm^{-1}	2.79592 $Å^{-1}$	2.24859 Å

potential minima, V_{min} (cm^{-1}), and normal-mode frequencies, $\hbar\omega$ (cm^{-1})

well	V_{min}	$V_{min} - V_{min}(C_6)$	$\hbar\omega$	zero-point energy
C_6	−5379	0	406, 173[a]	376
C_5	−5162	215	418, 113[a]	322

saddle-point energies, $V^{\ddagger}$(cm^{-1}), and normal-mode frequencies, $\hbar\omega$ (cm^{-1})

saddle	$V^{\ddagger}$	$V^{\ddagger} - V_{min}(C_6)$	$\hbar\omega$
C_6:C_5	−5078	301	430, 83, 23*i*
C_6:C_6	−5071	308	429, 70, 141*i*

[a] Doubly degenerate.

calculated along five, one-dimensional, radial cuts emanating from the C_{60} origin. The one-dimensional radial rays are each defined by the point at which they intersect the C_{60} cage. The five intersection points were as follows:

(1) the center of a C_6 ring,

(2) the center of a C_5 ring,

(3) the midpoint of a C−C bond forming the edge of one C_6 ring and one C_5 ring,

(4) the midpoint of a C−C bond forming the edge of two C_6 rings,

(5) and a C atom.

For rays (1) and (2), it was necessary to shift the intersection point slightly (0.1 au) off the center of the rings in order to reduce the symmetry to avoid problems caused by the occasional convergence to an excited electronic state. Because of the high (I_h) symmetry of the C cage, there are many rays within the system equivalent to the specific rays used. For example, there are 20 equivalent rays corresponding to ray (1), 12 equivalent rays corresponding to ray (2), and 60 equivalent rays corresponding to ray (5). Thus, these rays cover a large part of the actual potential surface when symmetry is considered. Rays (1), (2), and (4) also correspond to 3-, 5-, and 2-fold symmetry axes, respectively.

It turns out that when Li is at the center of the C_{60} cage, the potential is a local maximum, and we take this point to be the zero of energy. The potential energy range of interest for obtaining the lowest several hundred eigenstates is from −5400 to −4000 cm^{-1}. We find that the simple sum of Morse Li−C interactions,

$$V(x,y,z) = D_e \sum_{j=1}^{60} \{(1 - \exp[-\alpha_e(s_j - s_e])^2 - 1\} \qquad (2)$$

with $s_j = [(x - x_j)^2 + (y - y_j)^2 + (z - z_j)^2]^{1/2}$ being the distance between Li at position (x, y, z) and C atom j at (x_j, y_j, z_j), with just three parameters, D_e, α_e, s_e, fits our ab initio data with a root-mean-square (rms) error of 41 cm^{-1}. Of course, eq 2 should not be regarded as arising from any physical model of the bonding but as a simple few-parameter function that fits the data reasonably well. The Morse parameters are listed in Table 1. Use of a sum of Lennard-Jones interactions gives just a slightly worse rms error of 45 cm^{-1}. In view of the approximations in the underlying B3LYP calculations, further attempts to improve the accuracy of the fit are unwarranted.

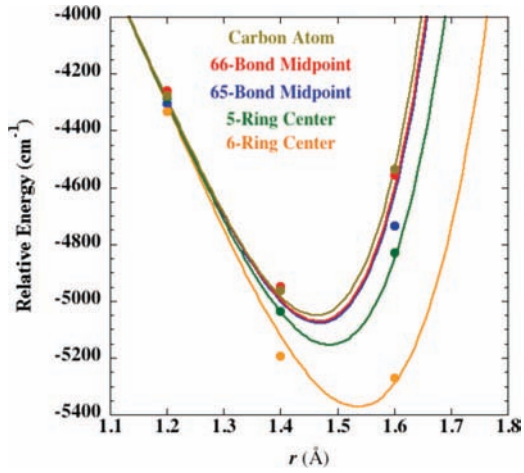

Figure 1. Potential-energy function (curves) evaluated along five one-dimensional rays in r, the distance of Li from the C_{60} center. Symbols are the DFT data, and the energy is relative to $r = 0$. The ray corresponding to Li approaching the center of a C_6 ring has the lowest minimum (yellow curve), followed by the ray corresponding to Li apporaching the center of a C_5 ring (green curve).

Figure 1 displays the DFT data (symbols) and potential-energy function fit (curves) for the five rays defined above. All the rays exhibit minima at ∼1.5 Å from the center of the C_{60} cage, and the maximum difference between minima (inferred from the fit) is just ∼330 cm^{-1}. The ray corresponding to Li approaching the center of a C_6 ring is lower in energy than any of the other rays, having a minimum ∼217 cm^{-1} below that of the next lowest ray, which corresponds to Li approaching the center of a C_5 ring. These are the two most important rays for understanding the lowest energy quantum states, and we will refer to the potential wells associated with them as the hexagonal and pentagonal wells. The other rays are fairly similar in energy. Although the fit is not perfect, these key features of the DFT data are reproduced by the simple potential form in eq 2, in particular the relative stabilities of the hexagonal and pentagonal wells. Other features of the potential will be discussed in Section 3 below. The energy scale of Figure 1 is relative to the energy of Li placed at the center of C_{60}. Relative to separated Li and C_{60}, the Li@C_{60} minimum is found to be ∼11 260 cm^{-1} lower in energy; that is, Li@C_{60} is stable relative to Li + C_{60}.

Two earlier DFT-based determinations of features of the Li@C_{60} potential[15,16] employed local density functional (LDF) theories, which are generally not as accurate as non-LDF theories,[20] such as the B3LYP DFT used here. Nonetheless, they lead to results that are consistent with our results in that they predict only weak deviations from spherical symmetry, and the magnitudes of their potential minima are comparable to ours. In ref 15, the relative difference between pentagonal and hexagonal minima was less (0.01 eV or 80 cm^{-1}) than ours (217 cm^{-1}), and furthermore, the pentagonal wells were the more stable ones. However, the magnitude of the potential minima relative to the center of the cage calculated with local DFT, ∼−4600 cm^{-1}, is only ∼700 cm^{-1} more shallow than our mean result (see Figure 1), ∼−5300 cm^{-1}. Regarding the other DFT study, it is difficult to infer relative stabilities from the figures and discussion of ref 16, but one can estimate that the various minima differ by no more than ∼0.1 eV or ∼800 cm^{-1}. The order of magnitude of the potential minima of ref 16 relative to the cage center is ∼−6400 cm^{-1}, that is, ∼1100 cm^{-1} deeper than our result. The differences between the relative energies from the two LDF-based DFT calculations and our B3LYP-based ones, on the order of 1100 cm^{-1} (0.1 eV) or less,

are probably not significant on the scale of the expected accuracy of LDF-based DFT.

2.2. Eigenvalue and Eigenvector Determinations. The Lanczos method[21,22] was used to determine both the lowest eigenvalues and the eigenvectors for the system. The details of our implementation of the Lanczos method, including how eigenvectors are obtained once the eigenvalues are known, are very similar to those of ref 22 and need not be repeated here. Rather than using a standard basis set representation that explicitly reflects the symmetry of the potential, we represent the wave function on a three-dimensional, evenly spaced, Cartesian grid. The wave function is then imagined to be expanded in terms of direct product states $|x_i>|y_j>|z_k>$ associated with the various (i, j, k) grid points.

In the Lanczos method, a three-term recursion involving repeated actions of a matrix representation of the Hamiltonian (**H**) on a vector (**q**), **Hq**, is required. With the three-dimensional Cartesian grid, the potential part of **H** is diagonal, and standard Fourier transform techniques[23] are used to evaluate the kinetic part. At various stages in the iterations, a tridiagonal matrix is constructed, and its energy levels converge to the true levels of **H**, that is, those satisfying

$$\mathbf{H}\Psi_n = E_n\Psi_n, \qquad n = 0, 1, ... \tag{3}$$

with the lowest and highest levels converging the earliest in the process.

A few additional remarks on the Hamiltonian matrix, **H**, and the evaluation of **Hq** are in order. If one has m evenly spaced grid points per degree of freedom, formally, **H** is an $N \times N$ matrix with $N = m^3$. The direct-product nature of the Cartesian representation is such that the number of nonzero matrix elements is far less than $N^2 = m^6$: each row of **H** has just $3m - 2$ nonzero matrix elements out of a possible m^3; therefore, the fraction of nonzero matrix elements is $\sim 3/m^2$. Moreover, with the Fourier method,[23] **Hq** is evaluated on the fly in a manner that does not require saving most of the matrix elements, and the numerical effort scales quasi-linearly with the number of grid points: if N_{op} is the number of operations for each evaluation of **Hq**, $N_{op} \propto N \log_2 m$.

The standard Lanczos method cannot resolve degeneracies because, by the nature of the process, it turns out that repeated copies of each correct eigenvalue arise no matter what the actual degeneracy of the eigenstate;[21] that is, there are numerous false degeneracies. Thus, one can infer what each energy level is but not its degeneracy from a standard Lanczos procedure. Reorthogonalized Lanczos methods could be used to remedy this defect.[24] We chose a less elegant but simple route, namely, to introduce a very small random perturbation into the problem that breaks the I_h symmetry and leads to nondegenerate (although closely spaced) eigenstates. The numbers of eigenstates in each cluster correspond to the degeneracy of the level and are consistent with the dimensions of the various representations of the icosahedral (I_h) group.

The random perturbation noted above corresponds to displacing each C atom in the cage as follows. For each C atom, $j = 1, 2, ..., 60$, the original, perfect icosahedral coordinates (x_j, y_j, z_j), as computed by the formula of ref 18 are replaced by

$$x_j \leftarrow x_j + (-1 + 2\xi_j^x)\eta$$

$$y_j \leftarrow y_j + (-1 + 2\xi_j^y)\eta$$

$$z_j \leftarrow z_j + (-1 + 2\xi_j^z)\eta \tag{4}$$

where η is the strength of the perturbation and ξ_j^x, ξ_j^y, ξ_j^z are pseudorandom numbers between 0 and 1.

We find that for $\eta \leq 10^{-7}$ Å, one obtains small clusters of energy states with the number of states in each cluster corresponding to one of the dimensions of the various representations of I_h. An interesting effect regarding the totally symmetric (nondegenerate) representation will be discussed later in Section 3.4. Had we adopted a symmetry-adapted basis set instead of the grid representation—for example a product basis involving the subset of spherical harmonics that belong to I_h and appropriate radial functions—we would not have found the effect discussed in Section 3.4.

We employ evenly spaced grids with 128 points in the range from −6.5 to 6.5 au for each of the three degrees of freedom. (Calculations with just 64 points per degree of freedom yield energy levels within 0.05 cm^{-1}.) The Lanczos calculations are readily carried out on an ordinary Intel-based PC or laptop computer, and the first few hundred levels converge within 1 h, whereas a full spectrum up to 950 cm^{-1} excitation energy, corresponding to the first 1200 states, can be calculated within a day. (In terms of the number of Lanczos iterations, which corresponds to the size of the Krylov space, and the tridiagonal matrix that leads to the energy levels, about 5000 iterations yield the first few hundred levels and about 50 000 iterations yield the first 1200 levels.) As noted above, subsequent Lanczos calculations are carried out to determine the eigenfunctions.

3. Results and Discussion

3.1. Potential Function. With origin at the center of the C_{60} cage, the Cartesian coordinate system used is oriented as that in ref 18. Then, the z axis passes through the centers of two opposite end pentagonal (C_5) rings, and the $x-z$ plane contains the centers of two connected hexagonal (C_6) rings in its lower right quadrant, as well as in the upper left quadrant. Spherical coordinates based on these Cartesian coordinates are defined with the convention that θ is the polar angle from the z axis, and ϕ is the azimuthal angle. The C_{60} cage has 20 hexagonal (C_6) and 12 pentagonal (C_5) rings. The top panel of Figure 2 is a polar plot of the potential at $r = 1.54$ Å, vividly illustrating the corresponding C_6 and C_5 potential wells, with the former being slightly deeper than the latter, as discussed in Section 2.2. The nature of such a polar plot distorts the wells so that equivalent wells have different shapes, and two of the pentagonal wells occur at the north and south poles of the sphere so that they are spread out over all ϕ at these points. Projections on the actual sphere do not have these distortions but are less informative because the back portion of the sphere is then hidden.

The lower panel of Figure 2 is a plot of the potential in the $x-z$ plane with $y = 0$. The specific orientation of our Cartesian coordinate system is such that this plane contains the rays associated with four of the C_6 ring centers and four of the C_5 ring centers. The potential wells corresponding to the C_6 ring centers are evident in the lower right and upper left quadrants, whereas the potential wells associated with the C_5 ring centers are in the upper right and lower left quadrants. These latter wells are shallower than the C_6 wells (Figure 1) and are less clearly seen in such an image map.

Further analysis of the potential function shows that only two of the minima with respect to r along the five rays in Figure 1 correspond to actual minima with respect to all coordinates. Two of the other rays correspond to saddle points, and one ray, ray (5), although still a stationary point, is neither a minimum nor a saddle point. Table 1 gives the properties of the minima and saddle points. There is a global minimum for the hexagonal wells with energy −5379 cm^{-1} at $r = 1.54$ Å and a slightly

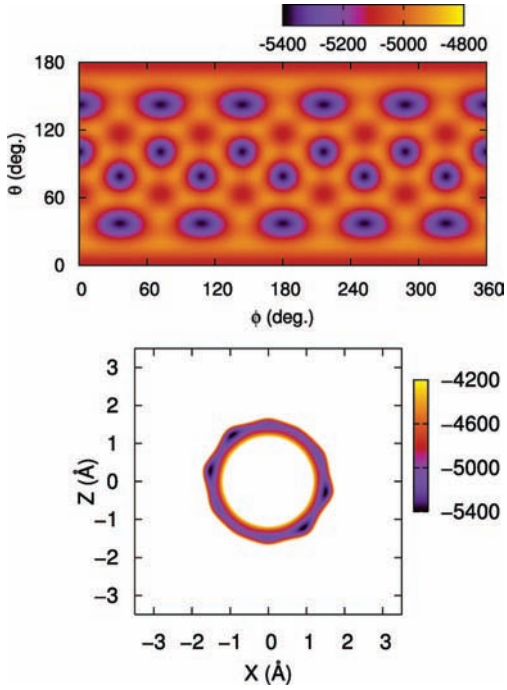

Figure 2. Image map of the potential-energy surface for Li in an angular shell with $r = 1.54$ Å from the cage center (top) and image map of the potential in the $x-z$ plane (bottom; white space means that the potential is higher than -4200 cm^{-1}). The unit of the color keys is cm^{-1}.

higher energy local minimum for the pentagonal wells with energy -5162 cm^{-1} at $r = 1.49$ Å. The minima with respect to r along the rays associated with Li approaching the centers of 5−6 and 6−6 bonds are actually saddle points or barriers between the wells and have energies of -5078 and -5071 cm^{-1}, respectively. This corresponds to barriers of 301 cm^{-1} for a Li to go from a hexagonal to a pentagonal well and 309 cm^{-1} to go between hexagonal wells. Relative to a pentagonal well, which is energetically higher than a hexagonal well, the barrier connecting it to a hexagonal well is only 84 cm^{-1}.

We have carried out a normal-mode analysis for the minima and saddle points. In all cases, the highest frequency mode, in the 400−430 cm^{-1} range, is the Li radial mode. In the case of the minima, there is a lower-frequency doubly-degenerate librational mode. As seen from the table, the hexagonal wells are slightly softer than their pentagonal counterparts in the radial direction but are significantly stiffer for the librational modes. Both wells are stiffer outwardly than inwardly, leading to anharmonicity in the radial vibrations. The normal-mode analysis and energies suggest that the lowest energy states should be hexagonal in character, but that pentagonal and mixed hexagonal/pentagonal states will exist at higher energies. The first radial vibration excitations should occur ∼376 cm^{-1} above the ground state.

3.2. Energy Levels. With the procedures discussed in Section 2.1, we determined the lowest 1200 eigenstates corresponding to excitation energies up to 950 cm^{-1}. Figure 3 shows an energy level stick diagram for Li@C_{60} inferred from the Lanczos calculations and contrasts it with that for a system of spherical symmetry where the radial potential has been taken to be that of the ray to the center of a hexagon. We see that the full Li@C_{60} system exhibits band structures that are distinct from the spherical case, essentially because of the icosahedral symmetry and multiple-well features of the potential which we will elaborate upon.

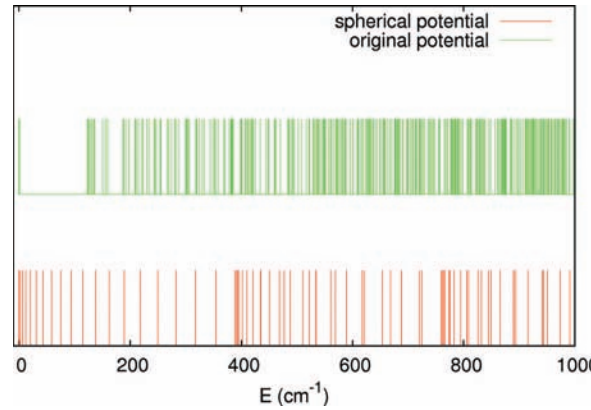

Figure 3. Stick spectrum of the Li@C_{60} energy levels determined with the full potential (upper, green) is contrasted with the results for a spherically symmetric potential (lower, red). The energies shown are relative to that of individual ground states.

Although not clearly evident in Figure 3 owing to the energy scale, there is actually a band of 20 states, with a width of ∼1 cm^{-1}, corresponding to the ground state at zero excitation energy. This band contains six distinct energy levels with degeneracies of 1, 3, 5, 4, 4, and 3 in energetic order, which is consistent with the dimensions (1, 3, 4, 5) of the various irreducible representations of the I_h point group.[17] Because there are 20 equivalent hexagonal wells, one can imagine this band as resulting from tunneling interactions between degenerate zero-order states centered on each well. We develop this tunneling picture more explicitly in the Appendix. This band structure, as well as a band gap associated with it, can also be modeled by exploiting the unique I_h symmetry of the potential, as shown in ref 17 where a two-dimensional model was considered. The ground state has zero-point energy $E_0 - V_{min} = -5023.0$ cm^{-1} $-$ ($-$ 5379.4) = 356.4 cm^{-1}, which compares favorably with the approximate normal-mode result, 376 cm^{-1}, from Table 1. Inspection of selected wave functions in Section 3.3 below will also verify and elaborate upon some of the assignments of this section.

After the very narrow first band, there is a gap of 121.7 cm^{-1} followed by a wider band of 40 states with energies ranging from 122.7 to 136.3 cm^{-1}. This band can be associated with the 40 states that would result from the first excitation of the doubly-degenerate librational mode in each of the 20 hexagonal wells. As with the ground-state band, all levels in this band have degeneracies corresponding to the dimension of an I_h irreducible representation, although in this case, there are no singly-degenerate levels. We note that anharmonic effects seem to be already quite important because the corresponding normal-mode frequency (Table 1) is considerably higher at 173 cm^{-1}.

Around an excitation energy of 150 cm^{-1}, we find a third band, with a width of ∼10 cm^{-1}, consisting of four distinct energy levels with degeneracies of 1, 3, 5, and 3 in increasing energetic order. Because there are 12 equivalent pentagonal wells, this band corresponds (mostly) to the ground state of the higher-energy, pentagonal wells. On the basis of Table 1, the zero-order excitation of this state would be 153 cm^{-1}, in agreement with the aforementioned results.

3.3. Eigenfunctions. We now examine several of the non-degenerate (A_g) eigenfunctions. Polar plots at the radius where the wave function reaches its maximum value are discussed, as well as cuts of the wave function in the $x-z$ plane with $y = 0$ defined in Section 2.2.

The top panel of Figure 4 shows a polar plot of the ground-state wave function, which is localized over each of the 20

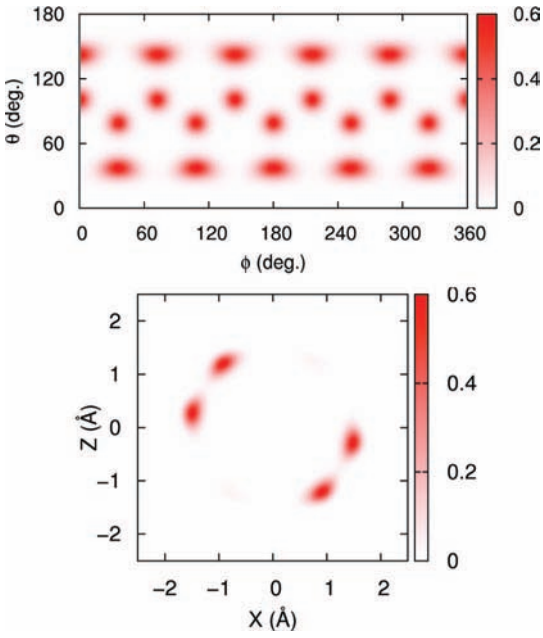

Figure 4. Polar and $x-z$ plane plots of the ground-state wave function. The wave-function amplitude scales are in atomic units.

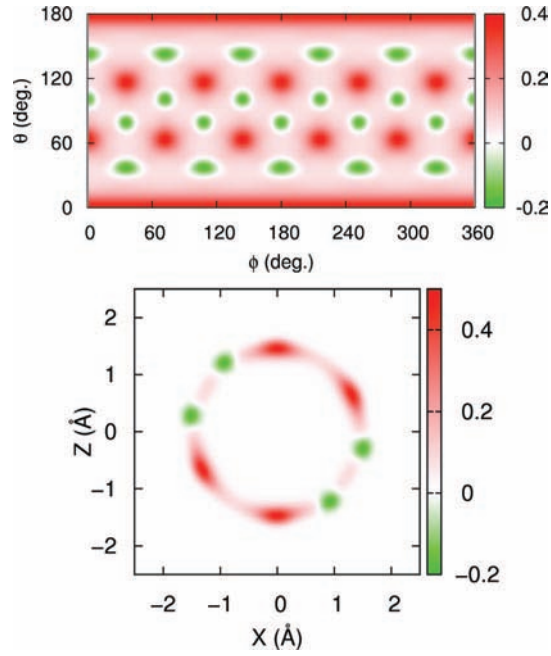

Figure 5. Polar and $x-z$ plane plots of the first excited nondegenerate state at an excitation energy of 150.4 cm^{-1}. The wave-function amplitude scales are in atomic units.

hexagonal wells. By assuming that the radial and librational motions are weakly coupled, we can subtract the approximate radial zero-point energy (~406/2 = 203 cm^{-1}) from the total zero-point energy of this state (356 cm^{-1}) to yield an effective energy of 153 cm^{-1} in the librational mode. This latter energy is insufficient to surmount the hexagon−hexagon and hexagon−pentagon barriers of 309 and 301 cm^{-1}, respectively. Thus, one would expect the ground state to consist of localized amplitude over each hexagonal well. Of course, tunneling between wells does occur and is responsible for the ground-state band of 20 states. The $x-z$ plane cut through the wave function in the lower panel of Figure 4 shows four lobes of large amplitude—two in the lower right quadrant and two in the upper left quadrant. The nature of this cut is such that there are hexagonal wells in these regions of large amplitude (Figure 2); therefore, this result is consistent with the assignment.

Figure 5 shows polar and $x-z$ plane plots of the first excited nondegenerate state, at an excitation energy of 150.4 cm^{-1}. This wave function exhibits significant localization in the pentagonal wells, consistent with the energy-level analysis in Section 3.2, where it was suggested it should be the lowest member of the band of ground-state pentagonal states. However, localization around the hexagonal wells is also clearly visible, although a little weaker. This is not surprising because the approximate effective energy in the librational mode (relative to the hexagonal well as zero) is ~356 + 150 − 203 = 303 cm^{-1} by using data from Tables 1 and 2. This energy is almost the same as the barrier height connecting pentagonal and hexagonal wells (301 cm^{-1}).

Figure 6 is a polar plot of the next nondegenerate state with an excitation energy of 197.7 cm^{-1}. Although still relatively low in energy, this state cannot easily be classified as involving just the hexagonal or just the pentagonal wells as the previous two states discussed could be. Rather, both the polar and $x-z$ plots show approximately equal (and in phase) amplitudes in both hexagonal and pentagonal wells. There is also significant amplitude, out of phase with respect to the amplitude over the wells, lying in the barrier regions between wells.

As is to be expected, most higher-energy states exhibit significantly more complex (but visually appealing) patterns than those discussed so far. It is possible, however, to assign some of the features in these patterns. Figure 7, for example, shows a state with an excitation energy og 413.4 cm^{-1}. Although the upper polar plot is rather complex, the lower $x-z$ cut exhibits a radial node in the upper left and lower right quadrants. This corresponds to one quantum of radial excitation coupled into the hexagonal angular excitations. Such states and the numerous others with radial-excitation character are relevant to interpreting the IR spectrum.

TABLE 2: Localization of the Ground-State Wave Function Due to Perturbation of the Cage Atoms

perturbation, η (Å)	potential spread, ΔV_{min} (cm^{-1})	localization, Δ
10^{-7}	0.0017	0.0006
10^{-6}	0.0012	0.0007
10^{-5}	0.0182	0.0061
10^{-4}	0.1674	0.0621
10^{-3}	1.6553	0.7996

3.4. Spectrum. A simple estimate of the IR absorption spectrum can be obtained from

$$I(E) = \sum_i \exp(-E_i/kT) \times \sum_j (\mu_{x,ji}^2 + \mu_{y,ji}^2 + \mu_{z,ji}^2)\delta(E - (E_j - E_i)) \quad (5)$$

where $\mu_{x,ji} = |\langle\psi_j|x|\psi_i\rangle|$ and so forth. In principle, the nuclear position-dependent electronic expectation value of the dipole operator should be used instead of x, y, and z. Examination of Mulliken populations showed that the ground-state wave function is essentially ionic in character ($Li^+C_{60}^-$), consistent with earlier calculations.[15,16] This justifies the use of the position vector as a surrogate for the dipole moment. (This approximation was validated by comparison with calculated dipole moments at selected points.) Equation 5 was evaluated by using all the calculated eigenfunctions for excitation energies <950 cm^{-1}, which is adequate for temperatures up to 300 K.

Figure 8 displays spectra for T = 300 (upper) and 10 K (lower), which are qualitatively similar with the higher-

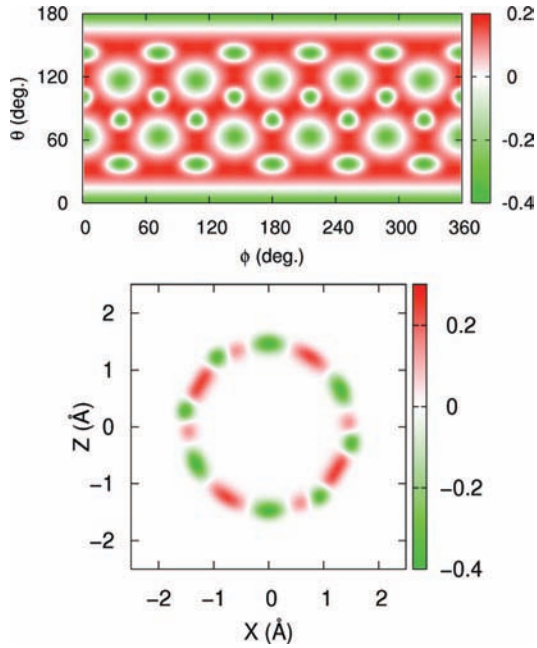

Figure 6. Polar and $x-z$ plane plots of the 197.7 cm^{-1} excitation-energy state. The wave-function amplitude scales are in atomic units.

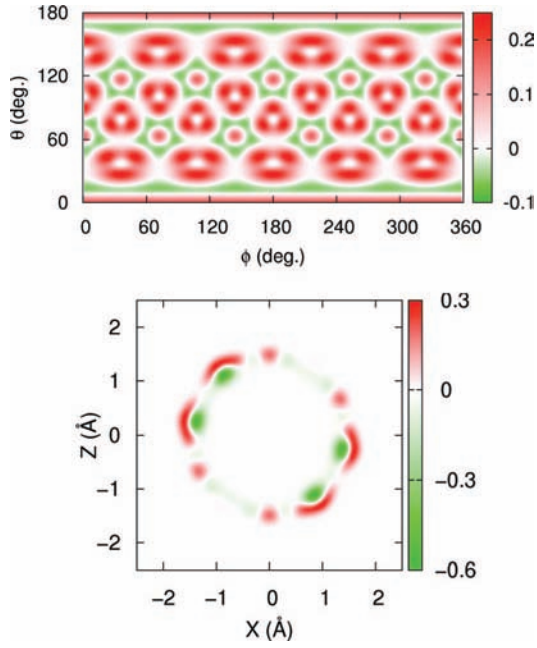

Figure 7. Polar and $x-z$ plots of the 413.4 cm^{-1} excitation-energy state, which exhibits nodes (lower panel) consistent with one quantum of radial excitation. The wave-function amplitude scales are in atomic units.

temperature spectrum being a little broader. There are prominent spectral structures around 125 and 400 cm^{-1}, which naturally must correspond to the first librational and radial excitations discussed in the previous sections. The experimental Li@C_{60} IR data[12–14] that we are aware of, unfortunately, correspond to excitation energies greater than 400 cm^{-1} and are complicated by a number of overlapping/coupled C_{60} cage vibrational excitations, as well as impurities. Also, C_{60} has a few IR modes in the spectral region of Figure 8.[25] The present result, which completely decouples the motion of Li from the cage-atom motions, represents a prediction of the Li motion contribution to the low-temperature/far-IR spectrum of Li@C_{60}. (It may be

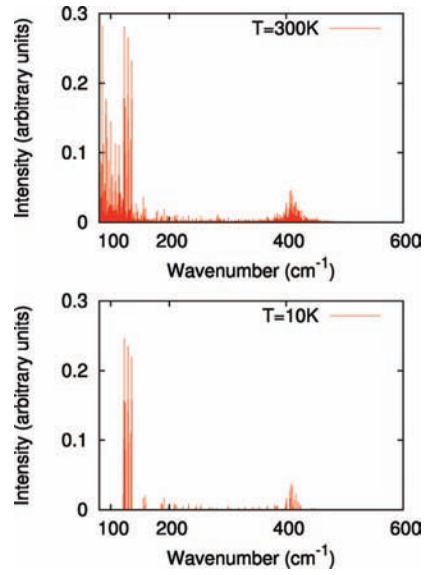

Figure 8. Far-IR absorption spectra for Li@C_{60} inferred from our calculations.

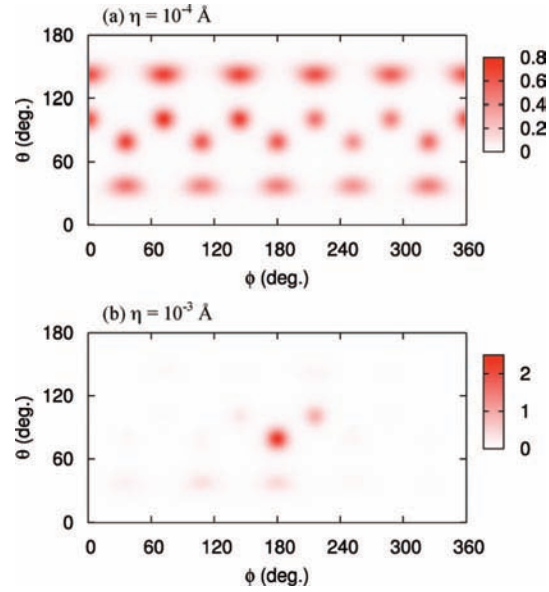

Figure 9. Localization of the ground state. (a) With $\eta = 10^{-4}$ Å, some unevenness becomes visible (the density of the most-dense well is more than three times that of the least-dense well). (b) With $\eta = 10^{-3}$ Å, the ground state is essentially localized in one well, completing the transition from an evenly distributed symmetry-preserving state to a strongly localized state completely lacking I_h symmetry. The wave-function amplitude scales are in atomic units.

of interest to also consider the Raman spectrum. See an earlier theoretical analysis of the Raman spectrum of Li^+@C_{60}.[26])

3.5. Symmetry Breaking Perturbations. The introduction of a small ($\eta \leq 10^{-7}$ Å) perturbation proved to be a very useful device for deducing degeneracies from the results of our Lanczos calculations. However, it is interesting to note that the ground-state wave function deviates drastically from I_h symmetry as somewhat larger but still small perturbations are applied to the positions of the C atoms. In the calculations that we now discuss, a random perturbation is imposed in the same way as that specified in eq 4. In Figure 9, we display polar plots of the wave function ($r = 1.54$ Å) for perturbation levels $\eta = 10^{-4}$ Å (upper panel) and $\eta = 10^{-3}$ Å (lower panel). These results should be compared with those for the unperturbed cage, Figure 4. Some deviation from symmetry is evident at the $\eta = 10^{-4}$ Å

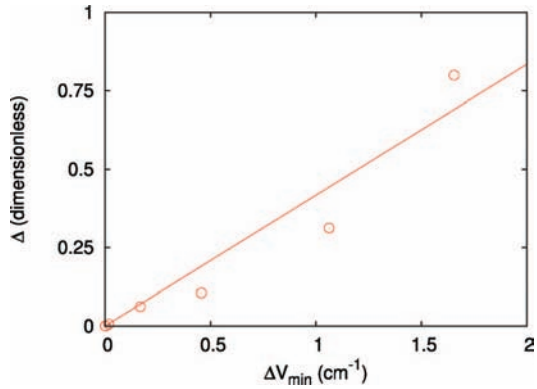

Figure 10. Degree of localization, Δ, for different levels of perturbation of the potential (measured by ΔV_{min}).

level, but quite remarkably, the $\eta = 10^{-3}$ Å level is completely localized. Of course, different random-number sequences will give different results, for example, localization in different wells. However, the qualitative features of the localization remain the same.

Because the ground state is mostly confined to the 20 hexagonal wells, evenly in the unperturbed case, we consider the probability associated with each of these wells by integrating the square of the wave function over a cone that just encompasses the well. The maximum of these 20 probabilities, minus the minimum, which we call Δ, is one measure of localization. In the unperturbed case, the probability of occupation of each well is 1/20, and $\Delta = 0$. In the case of complete localization in a single hexagonal well, $\Delta = 1$. For each random perturbation, η, the well depths of the 20 hexagonal wells are somewhat changed. Let ΔV_{min} be the corresponding largest well depth minus the smallest well depth. Table 2 presents values for η, ΔV_{min}, and Δ. For $\eta = 10^{-4}$ Å, we find $\Delta V_{min} = 0.17$ cm^{-1}, and for $\eta = 10^{-3}$ Å, we find $\Delta V_{min} = 1.65$ cm^{-1}. In Figure 10, we plot the degree of localization, Δ, versus the spread in potential minima, ΔV_{min}. As might be expected on the basis of first-order perturbation theory, there is an approximate linear relation between Δ and ΔV_{min}.

From Figure 9, it is clear that the localization of the wave function becomes noticeable near $\Delta V_{min} = 0.17$ cm^{-1} ($\eta = 10^{-4}$ Å) and becomes extreme by $\Delta V_{min} = 1.67$ cm^{-1} ($\eta = 10^{-3}$ Å). The potential energy spread of $\Delta V_{min} = 0.17$ cm^{-1} is comparable to the half tunneling splitting $(1/2)\Delta E_{tun}$ of 0.18 cm^{-1}, calculated in the Appendix. Thus, a rough criterion for the localization effect to become important is simply $\Delta V_{min} > (1/2)\Delta E_{tun}$. The localization effect noted here, although in relation to the quantum states of a relatively small molecule, bears similarities to Anderson localization[27–30] in the solid state. In particular, they share a similar localization criterion if we associate ΔV_{min} with the spread of site energy levels due to an impurity, W, in the Anderson model and associate $(1/2)\Delta E_{tun}$ with the hopping energy, V, noting that the strong localization happens when W/V becomes larger than a system-specific number, which is on the order of 1−10 in two dimensions.

The extreme sensitivity to small perturbations only exists for the ground state in our system. As discussed previously, different rotation bands mix heavily beyond the first band of 20 states that corresponds to localization in the 20 hexagonal wells. Therefore, the threshold for symmetry breaking, approximately proportionate to the bandwidth, is much larger beyond the first band. It should also be noted that such a localization effect is hardly observable at room temperature because the energy splitting between different localization scenarios is so small that any such effect is smeared out by thermal fluctuations. For sufficiently low temperatures, however, the effect may be observable. In this limit, temporary deformations of C_{60} could lead to a localization of Li atom, which in turn, by essentially ionic interaction with the cage, could lock in the deformation and induce a simultaneous symmetry breaking. Another possible scenario can be envisaged for a hypothetical crystal of Li@C_{60} molecules, where various breathing modes of the cage can be propagated in waves. It is plausible that a polaron-like quasiparticle can emerge because of the ability of the Li ion to localize and deform the surrounding cage. However, an actual calculation of this effect would demand a detailed study of the coupling of the motion of the Li ion/atom and the cage, which is beyond the scope of this study.

4. Summary

We have reported the results of a study of a simple three-dimensional model for Li moving inside a rigid C_{60} cage. The system exhibits an interesting potential topography with 20 equivalent wells associated with Li being under a hexagon in the cage and 12 equivalent wells associated with Li being under a pentagon in the cage. Our potential model was based on DFT calculations more accurate than those previously carried out for this system. Although still not of spectroscopic accuracy, our model is likely more reflective of the true nature of the system's dynamics. We used this potential to determine hundreds of ro-vibrational Li@C_{60} quantum states, which represent the first fully three-dimensional ro-vibrational states obtained for this system. We also made a prediction of the far-IR spectrum and examined the nature of selected eigenfunctions. Finally, we showed that small perturbations of the cage-atom positions can have a dramatic effect on the nature of the ground-state wave function.

Our quantum calculations of the system eigenstates also revealed that even at very low excitation energies, the wave function is a complex superposition of hexagonal, pentagonal, and possibly barrier states. We believe, apart from any connections with actual Li@C_{60} molecules, that this model is an excellent one for studying multiple-well dynamics in general. In the future, we plan to study the corresponding classical dynamics of the system and, within that limit, to introduce cage-atom motions.

Appendix: Tunneling Splitting and Bandwidth

To solidify the assertion that the lowest band of 20 Li@C_{60} quantum states arises from tunneling between the hexagonal wells, we present a simple tunneling model to approximate the bandwidth. This model corresponds to a 20 × 20 Hamiltonian matrix imagined to be formed from a basis of single-well states. The diagonal elements are all the same and equal to the zero-point energy associated with a single well, ε_0. Each of the 20 hexagons in C_{60} has three hexagonal neighbors, and we assume that only matrix elements between such nearest neighbors are nonzero. That is, given a specific choice of numbering the 20 hexagonal wells, each row of the Hamiltonian matrix has three off-diagonal elements corresponding to its three nearest-neighbor wells. We take these off-diagonal matrix elements to be $-\gamma$, where γ will be associated with a tunneling splitting. Diagonalization of this model Hamiltonian yields the same degeneracies (1, 3, 5, 4, 4, 3) and similar energy scalings as those calculated by the Lanczos method for the full problem. The bandwidth resulting from this model is 5.24γ.

For a symmetric double-well potential $V(x)$, the WKB approximation for the energy splitting between the lowest two

states due to tunneling is[31] $\Delta E_{tun} = (\hbar\omega/\pi)e^{-\theta}$, where ω is the classical angular frequency of an individual well and θ is the tunneling integral, $\theta = (1/\hbar)\int_a^b dx\ [2m(V - \varepsilon_0)]^{1/2}$, where the integration is over the barrier region with $V > \varepsilon_0$ and a and b are the turning points such that $V(a) = V(b) = \varepsilon_0$. We take x to be the distance traveled along the most energetically favorable path linking two C_6 minima. In the present case, we have $\hbar\omega = 173\ cm^{-1}$, $\varepsilon_0 = \hbar\omega/2 = 86.5\ cm^{-1}$, and a barrier height of 308 cm^{-1} (Table 2). A straightforward numerical calculation yields $\Delta E_{tun} = 0.26\ cm^{-1}$.

In the case of just two degenerate states coupled by the matrix element $-\gamma$, the splitting of the levels is 2γ. We therefore take the nearest-neighbor interaction in our 20×20 model Hamiltonian to be $\gamma = \Delta E_{tun}/2 = 0.13\ cm^{-1}$. This is within a factor of 2 of the value $\gamma = 0.18\ cm^{-1}$ which would exactly reproduce the bandwidth from our full Lanczos calculations. The resulting model bandwidth is 0.68 cm^{-1}, compared to the full Lanczos result of 0.95 cm^{-1}.

Acknowledgment. The work at Argonne National Laboratory was supported by the U.S. Department of Energy, Basic Energy Sciences, under contract no. DE-AC02-06CH11357. We also acknowledge support from the Joint Theory Institute, a University of Chicago and Argonne National Laboratory multidisciplinary research institution.

References and Notes

(1) Bethune, D. S.; Johnson, R. D.; Salem, J. R.; De Vries, M. S.; Yannoni, C. S. *Nature* **1993**, *366*, 123.
(2) Shinohara, H. *Rep. Prog. Phys.* **2000**, *63*, 843.
(3) Dunsch, L.; Yang, S. *Phys. Chem. Chem. Phys.* **2007**, *9*, 3067.
(4) Kobayashi, S.; Mori, S.; Iida, S.; Ando, H.; Takenobu, T.; Taguchi, Y.; Fujiwara, A.; Taninaka, A.; Shinohara, H.; Iwasa, Y. *J. Am. Chem. Soc.* **2003**, *125*, 8116.
(5) Harneit, W. *Phys. Rev. A* **2002**, *65*, 032322.
(6) Komatsu, K.; Murata, M.; Murata, Y. *Science* **2005**, *307*, 238.
(7) Johnson, J. K.; Wang, Q. Y. *J. Phys. Chem. B* **1999**, *103*, 4809.
(8) Tun, L.; Goldfield, E. M.; Gray, S. K. *J. Phys. Chem. B* **2006**, *110*, 1742.
(9) Pan, X.; Fan, Z.; Chen, W.; Ding, Y.; Luo, H.; Bao, X. *Nat. Mater.* **2007**, *6*, 507.
(10) Tun, L.; Goldfield, E. M.; Gray, S. K. *J. Phys. Chem. C* **2008**, . in press.
(11) Xi, M.; Sebastianelli, F.; Bacic, Z.; Lawler, R.; Turro, N. J. *J. Chem. Phys.* **2008**, *128*, 011101.
(12) Tellgmann, R.; Krawez, N.; Lin, S.-H.; Hertel, I. V.; Campbell, E. E. B. *Nature* **1996**, *382*, 407.
(13) Krawez, N.; Tellgmann, R.; Gromov, A.; Kratschmer, W.; Campbell, E. E. B. In *Molecular Nanostructures;* Kuzmany, H., Fink, J., Mehring, M., Roth, S., Eds.; World Scientific: Singapore, 1997; pp 184−188.
(14) Gromov, A.; Ostrovskii, D.; Lassesson, A.; Jonsson, M.; Campbell, E. E. B. *J. Phys. Chem. B* **2003**, *107*, 11290.
(15) Dunlap, B. I.; Ballester, J. L.; Schmidt, P. P. *J. Phys. Chem.* **1992**, *96*, 9781.
(16) Li, Y. S.; Tomanek, D. *Chem. Phys. Lett.* **1994**, *221*, 453.
(17) Hernandez-Rojas, J.; Ruiz, A.; Breton, J.; Gomez LLorente, J. M. *Int. J. Quantum Chem.* **1997**, *65*, 655.
(18) Senn, P. *J. Chem. Educ.* **1995**, *72*, 302.
(19) Frisch, M. J.; Trucks, G. W.; Schlegel, H. B.; Scuseria, G. E.; Robb, M. A.; Cheeseman, J. R.; Zakrzewski, V. G.; Montgomery, J. A., Jr.; Stratmann, R. E.; Burant, J. C.; Dapprich, S.; Millam, J. M.; Daniels, A. D.; Kudin, K. N.; Strain, M. C.; Farkas, O.; Tomasi, J.; Barone, V.; Cossi, M.; Cammi, R.; Mennucci, B.; Pomelli, C.; Adamo, C.; Clifford, S.; Ochterski, J.; Petersson, G. A.; Ayala, P. Y.; Cui, Q.; Morokuma, K.; Malick, D. K.; Rabuck, A. D.; Raghavachari, K.; Foresman, J. B.; Cioslowski, J.; Ortiz, J. V.; Stefanov, B. B.; Liu, G.; Liashenko, A.; Piskorz, P.; Komaromi, I.; Gomperts, R.; Martin, R. L.; Fox, D. J.; Keith, T.; Al-Laham, M. A.; Peng, C. Y.; Nanayakkara, A.; Gonzalez, C.; Challacombe, M.; Gill, P. M. W.; Johnson, B. G.; Chen, W.; Wong, M. W.; Andres, J. L.; Head-Gordon, M.; Replogle, E. S.; Pople, J. A. *Gaussian 98*, revision A.7; Gaussian, Inc.: Pittsburgh, PA, 1998.
(20) Ziegler, T. *Chem. Rev.* **1991**, *91*, 651.
(21) Cullum, J.; Willoughby, R. A. *J. Comput. Phys.* **1981**, *44*, 329.
(22) Gray, S. K.; Goldfield, E. M. *J. Phys. Chem. A* **2001**, *105*, 2634.
(23) Kosloff, R.; Kosloff; D, *J. Chem. Phys.* **1983**, *79*, 1823.
(24) Baglama, J.; Calvetti, D.; Reichel, L. *BIT* **1996**, *36*, 400.
(25) Martin, M. C.; Du, X.; Kwon, J.; Mihaly, L. *Phys. Rev. B* **1994**, *50*, 173.
(26) Joslin, C. G.; Gray, C. G.; Goldman, S.; Yang, J.; Poll, J. D. *Chem. Phys. Lett.* **1993**, *215*, 144.
(27) Anderson, P. W. *Phys. Rev.* **1958**, *109*, 1492.
(28) Thouless, D. J. *Phys. Rep.* **1974**, *13*, 93.
(29) Economou, E. N.; Cohen, M. H. *Phys. Rev. B* **1972**, *5*, 2931.
(30) Bishop, A. R. *Phil. Mag.* **1973**, *27*, 651.
(31) Landau, L. L.; Lifshitz, E. M. *Quantum Mechanics*; Pergamon: New York, 1977.

JP801083M